Journal of ELECTRONIC MATERIALS, Vol. 47, No. 3, 2018
https://doi.org/10.1007/s11664-017-6025-4

Electric, Magnetic, and Magnetoelectric Properties of Yttrium-Containing $BaY_{0.025}Ti_{0.9625}O_3$–$SrFe_{12}O_{19}$ Composite

MEHRAJ UD DIN RATHER,[1] RUBIYA SAMAD,[1] and BASHARAT WANT [1,2]

1.—Solid State Research Lab, Department of Physics, University of Kashmir, Srinagar 190006, India. 2.—e-mail: basharatwant@gmail.com

The physical properties of $BaY_{0.025}Ti_{0.9625}O_3$, $SrFe_{12}O_{19}$, and $0.90BaY_{0.025}Ti_{0.9625}O_3$–$0.10\ SrFe_{12}O_{19}$ composite have been studied. The proposed composite was synthesized by solid-state reaction method from yttrium barium titanate processed by solid-state reaction and strontium hexaferrite obtained by a sol–gel process. Microstructural analysis revealed monophasic grains for yttrium barium titanate phase, while loosely packed biphasic structure was observed for the composite. Powder x-ray analysis showed that the individual phases retained their crystal structure in the composite, without formation of any new additional phase. Measurement of magnetic hysteresis loops at room temperature indicated that the magnetic parameters of the composite were diluted by the presence of the ferroelectric phase. The ferroelectric hysteresis of yttrium barium titanate confirmed the ferroelectric transition at 119°C. Meanwhile, the symmetrical ferroelectric loops observed at different fields established the ferroelectric nature of the composite. Improved dielectric properties and low dielectric losses were observed due to yttrium doping in the composite. The diffuseness of the ferroelectric transitions for the composite was confirmed by the Curie–Weiss law. Activation energy calculations revealed the charge-hopping conduction mechanism in the composite. Magnetodielectric studies confirmed that the overall magnetocapacitance in the composite exhibited combined effects of magnetoresistance and magnetoelectric coupling.

Key words: Multiferroics, phase transition, hopping mechanism, magnetodielectric

INTRODUCTION

The discovery of multifunctional materials has led to fascinating research activities in the present-day technological world.[1–3] Among the various multifunctional materials, multiferroic materials (MFMs) combine two or more ferroic orders (ferroelectricity, ferromagnetism, and ferroelastic) in the same phase. Ferroic materials have various internal switchable parameters which can be controlled using an external field. In ferroelectrics, the polarization can be switched using an electric field, while in ferromagnetic materials, the magnetization can be switched using a magnetic field.[3] The increasing interest in MFMs arises from the possibility to switch multiple ferroic degrees of freedom, which enables exciting innovations based on use of ferroelectric and ferromagnetic materials in novel data-storage devices, where opposite orientations of polarization or magnetization represent "1" and "0" data bits.[4,5]

Coexistence of ferroelectricity and magnetism in single-phase MFMs is rare and usually found at low temperatures.[6] Among the disadvantages of single-phase MFMs are high leakage current, high dielectric loss, and very low magnetoelectric coupling. In addition, the crystal structure must fulfill symmetry

(Received June 21, 2017; accepted December 12, 2017; published online December 20, 2017)

conditions and the structural building blocks should allow movement of ferroelectric ions.[7] To combine ferroelectricity and magnetism, multiferroic composites (MFCs) serve as potential candidates. The peculiar property of such MFCs is the coexistence of various ferroic orders above room temperature.[8–10] The favorable dielectric, ferroelectric, and magnetic properties observed in MFCs above room temperature have motivated further research by the scientific community. The most widely studied composites are made using lead zirconate titanate (PZT), $BaTiO_3$, and polyvinylidene fluoride (PVDF) as ferroelectric phase and $NiFe_2O_4$, $CoFe_2O_4$, $MnFe_2O_4$, $ZnFe_2O_4$, $BaFe_{12}O_{19}$, and $SrFe_{12}O_{19}$ as ferrite phase.[11–14] In our recent work, we reported coexistence of ferroelectric and ferromagnetic properties in $BaTiO_3$–$BaFe_{12}O_{19}$ composite at room temperature.[15]

Barium titanate (BT) is the most common ferroelectric oxide with perovskite ABO_3 structure and has peculiar electric properties. The interesting properties of BT, such as high dielectric constant, low dielectric loss, and fine tunability, make it a high-performance electronic material for application in electronic devices.[16] To enhance its dielectric and ferroelectric properties and reduce the dielectric loss, rare-earth ions can be doped in the crystal lattice of barium titanate.[17,18] Regarding the magnetic phase, strontium hexaferrite ($SrFe_{12}O_{19}$) is an important hard-magnetic material with ferrimagnetic structure in the M-type family. Its unique magnetic properties make it suitable for use in data storage and electronic devices.[19] All of these innovative applications based on $SrFe_{12}O_{19}$ are favorable at nanoscale range, where magnetic properties are strongly dependent on its nanostructure size, shape, orientation, and domain configurations.[20,21]

In the present work, we prepared yttrium-doped barium titanate (YBT) ferroelectric phase by solid-state reaction method. The aim of incorporating yttrium into the barium titanate lattice is to enhance its dielectric properties and reduce the transition temperature. $SrFe_{12}O_{19}$ (SHF) prepared by sol–gel autocombustion method was chosen as the second ferroic phase. The sol–gel method was adopted to obtain SHF grains of nanometer size, so that they could fit well in the voids of YBT phase. Detailed study of the ferroic properties of the composite fabricated from these ferroic materials is not prominent in literature. Thus, the dependence of the dielectric properties of the YBT–SHF composite over wide ranges of temperature and frequency was investigated in detail in this work. The variation of the alternating-current (AC) conductivity of the composite as a function of temperature at selected frequencies was also studied. In addition, the ferroelectric and ferrimagnetic properties of the composites were analyzed by recording respective hysteresis loops. Magnetodielectric (MD) studies were carried out at room temperature to confirm the magnetoelectric coupling in the composite.

EXPERIMENTAL PROCEDURES

Sample Preparation

Yttrium-doped barium titanate ceramic with nominal composition $BaY_{0.025}Ti_{0.9625}O_3$ was synthesized by solid-state reaction method. Stoichiometric amounts of high-purity $BaCO_3$ (99%), TiO_2 (99%), and Y_2O_3 (99.9%) were mixed in an agate mortar for 12 h. Acetone was used to homogenize the mixture, and the resulting mixture was calcined at 1100°C for 4 h with heating rate of 5°C/min and finally allowed to cool naturally. The calcined mixture was then ground to fine powder and sintered at 1300°C for about 24 h to produce fine $BaY_{0.025}Ti_{0.9625}O_3$ (YBT). Strontium hexaferrite (SHF) was prepared by sol–gel autocombustion method from analytical-grade chemicals including ferric nitrate nonahydrate, strontium nitrate anhydrous, and anhydrous citric acid. Metal nitrates and citric acid were dissolved in deionized water separately. The resulting solutions were mixed together at room temperature, with constant stirring, to form homogeneous solution. To maintain the pH of the solution at 7, ammonia solution was added dropwise to the mixture. The resulting solution was heated at 90°C to ensure gel formation, and the resulting gel was heated until combustion occurred, leaving ash behind. The obtained ferrite ash was ground using a motor and pestle for about 1 h. Finally, the powder was sintered at 950°C for 3 h for proper phase formation. Sintering was carried out in an electric furnace with alumina insulation boards as chamber walls. The thermal regime of the furnace was fully controlled using a Eurotherm programmer-cum-controller. For preparation of YBT–SHF composite, 90% YBT and 10% SHF phases by weight were mixed in an agate mortar for 3 h. The prepared ferroics, as well as YBT–SHF composite, were pressed into pellets with diameter of 13 mm under pressure of 155 kg/cm^2 using an automatic KBr press. Poly vinyl alcohol (PVA) was used as a binder for the formation of pellets. To enhance the density and avoid cracking, the resulting mixture in pellet form was sintered at 1150°C for 4 h, covering the pellets with powder of the same material in alumina crucible trays. The whole synthesis process is presented as a flowchart in Fig. 1.

Characterization

Complete information regarding the formation of the composite at room temperature was obtained by powder x-ray diffraction (XRD) analysis using a laboratory diffractometer with Cu K_α (λ = 1.5406 Å) radiation. Data were recorded in the range of $20° \le \theta \le 80°$ at scan rate of 0.020° per step and count time of 31.2 s per step. Scanning electron microscopy (SEM, Hitachi S-3000H) was used to study the morphology of the YBT, SHF, and YBT–SHF composite. As-sintered pellets were painted with silver for electrical measurements. To ensure good adherence of the electrodes to the ceramic, the

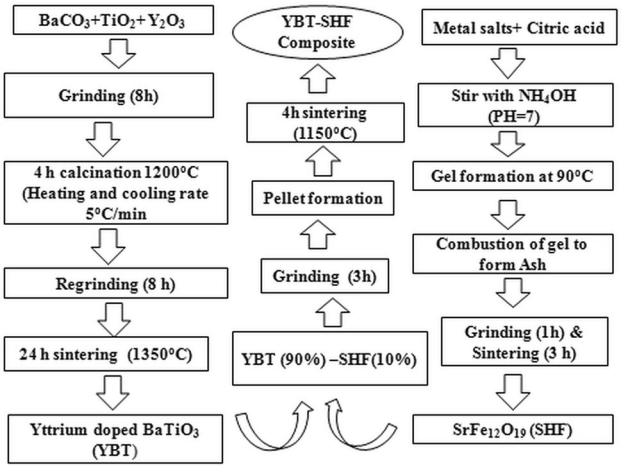

Fig. 1. Flowchart for synthesis of YBT phase, SHF phase, and YBT–SHF composite.

silver-painted pellets were heat-cured at 500°C for 1 h. The dielectric constant as a function of temperature (from 20°C to 450°C) at different frequencies (from 100 Hz to 1 MHz) and the frequency dependence of the dielectric constant and loss tangent at room temperature were determined using an impedance analyzer (model 6440B precision component analyzer, Wayne Kerr Electronics). The higher temperature required for dielectric studies was achieved using a microprocessor-based furnace fitted with a temperature controller and specially designed two-terminal sample holder. Electric hysteresis loops were traced using a modified Sawyer–Tower circuit (automatic *P–E* loop tracer, Marine India).

Magnetic measurements were carried out using a vibrating-sample magnetometer (EZ9 VSM, MicroSense, USA). Room-temperature magnetocapacitance was measured on silver-coated pellets (area 132 mm^2, thickness 1 mm) using a horizontal uniform magnetic field. Capacitance was measured at various frequencies (1 kHz to 3 MHz) with the sample plane parallel to the magnetic field.

RESULTS

Microstructure Observations

The microstructure of sintered disks of YBT, SHF, and YBT–SHF composite is shown in Fig. 2a, b, and c. Microstructural analysis of YBT revealed dense monophasic ceramic, consistent with the XRD results ("X-ray Diffraction Studies" section). The average grain size of YBT sintered at 1300°C ranged from 4 μm to 5 μm, while the particle size of SHF was about 56 nm (Fig. 2d). The surfaces of the YBT grains with size of $\sim$ 4.5 μm were connected together, confirming its high density (4.72 g/cm^3) compared with the YBT–SHF composite (4.6 g/cm^3). This high density is attributed to the lower mobility of Y^{3+} ions because of their larger ionic radius and atomic weight compared with Ti^{4+} ions.[22] Loosely packed biphasic structure was clearly observed for the composite, with SHF grains coalesced together with closely packed YBT grains because of the high temperature (1150°C).

Energy-dispersive x-ray spectroscopy (EDS) analysis was also carried out for the YBT–SHF composite to confirm the presence of various elements. Figure 3 clearly shows that all expected elements, including yttrium, were present in the composite.

X-ray Diffraction Studies

XRD patterns of sintered powder of YBT, SHF, and YBT–SHF composite are shown in Fig. 4, indicating that YBT crystallized in tetragonal perovskite structure. Perovskite phase of YBT with tetragonal crystal structure in space group *P4mm* (no. 99) matches with the standard value for $BaTiO_3$ in Joint Committee on Powder Diffraction Standards (JCPDS) card no. 50626, confirming entry of Y^{3+} ions into the unit cell while maintaining the perovskite structure.[23] The lattice constants a and c determined from XRD data for YBT were 3.994 Å and 4.033 Å, respectively. A slight increase in a accompanied by a decrease in c was observed compared with the theoretical values for pure $BaTiO_3$.[24] This change in the lattice constants of YBT can be attributed to the fact that the ionic radius of Ti^{4+} ion is smaller than that of Y^{3+} ion, so replacement of Ti^{4+} by Y^{3+} ions results in expansion of the unit cell.[25]

Based on the results for the composite, it is evident that YBT retained its tetragonal perovskite structure. The powder x-ray patterns revealed coexistence of the two ferroic phases with a high degree of sintering without any additional impurity phases. In the composite, the intensity of YBT peaks from planes such as (001), (101), (111), (200), (102), (211), (103), and (313) decreased on addition of SHF phase, as depicted in Fig. 4.

The phase fractions of YBT and SHF in the composite were calculated by using the intensity of the most intense peak of the XRD pattern of the two phases using the following equations:

$$\text{Phase percentage of SHF} = \frac{I_{\text{SHF}}}{I_{\text{SHF}} + I_{\text{YBT}}}, \quad (1)$$

$$\text{Phase percentage of YBT} = \frac{I_{\text{YBT}}}{I_{\text{YBT}} + I_{\text{SHF}}}, \quad (2)$$

where I_{YBT} and I_{SHF} are the intensity of the highest peak for YBT and SHF, respectively. The resulting phase fraction values (%) for the individual phases were consistent with those used during synthesis.

Evaluation of Densities

The bulk density (ρ_B) and corresponding porosity (γ) for YBT and SHF (Table I) were evaluated using the following relations[26]:

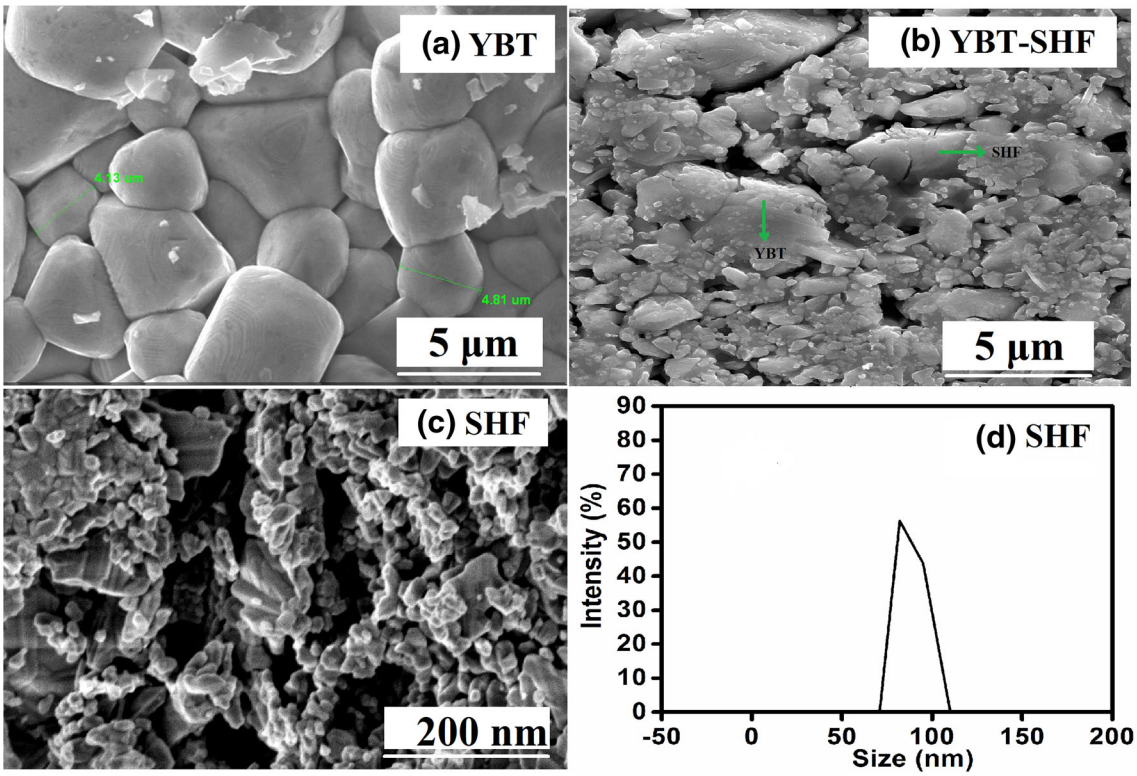

Fig. 2. SEM images at magnification of ×4000: (a) YBT phase, (b) SHF phase, and (c) YBT–SHF composite, and (d) particle size of SHF phase.

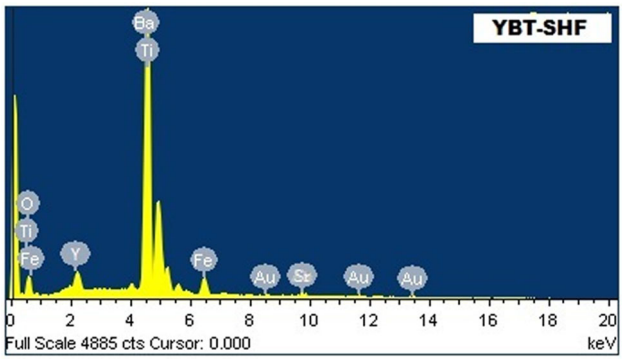

Fig. 3. EDS spectrum of YBT–SHF composite.

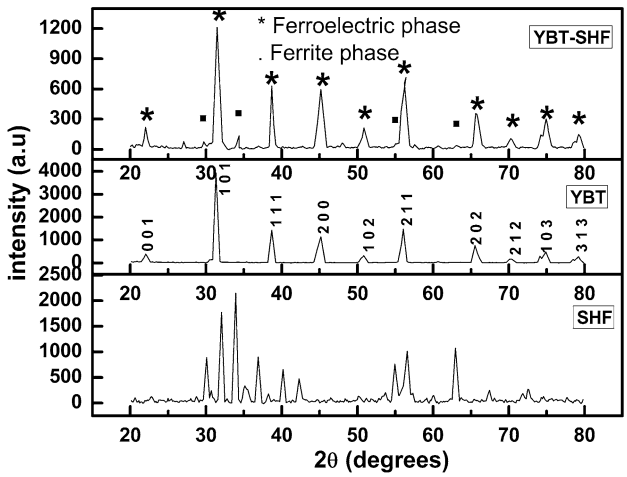

Fig. 4. X-ray diffraction patterns of YBT phase, SHF phase, and YBT–SHF composite.

$$\rho_B = \frac{M}{V}, \tag{3}$$

$$\gamma = 1 - \frac{\rho_B}{\rho_X}, \tag{4}$$

where M and V are the mass and volume of YBT and SHF, respectively. The x-ray density (ρ_X) for YBT and SHF was evaluated using the relation

$$\rho_{X=\frac{M'Z}{V_{cell}N_A}}, \tag{5}$$

where M' is the molecular weight, Z is the number of molecules per unit cell, V_{cell} is the volume of the unit cell, and N_A is Avogadro's number (6.023×10^{23}). The cell volume of SHF was calculated using the formula $V_{cell} = 0.8666a^2c$.[27] The bulk density of YBT disks sintered at 1350°C was lower than the corresponding x-ray density but greater than that of previously prepared pure barium titanate.[15] The bulk density of SHF (4.36 g/cm^3) was close to (85% of) the x-ray density (5.098 g/cm^3) of SHF. The difference between the bulk and x-ray densities is due to the porosity of the material. The porosity in the samples can be

Table I. Density, porosity, and magnetic parameters of YBT phase, SHF phase, and YBT–SHF composite

Sample	ρ_B (g/cm^3)	ρ_X (g/cm^3)	γ (%)	I_{YBT} (%)	I_{SHF} (%)	M_s (emu/g)	M_r (emu/g)	H_c (Oe)	M_r/M_s	n_B
YBT	4.72	5.16	8.53	–	–	–	–	–	–	–
SHF	4.36	5.09	14.35	–	–	59.30	32.31	6145	0.55	11.27
YBT–SHF	4.60	5.83	21.1	89.16	10.84	5.70	2.31	1622	0.40	1.07

attributed to the polymeric binder PVA, which burns out during sintering, leading to formation of open pores in the microstructure.[28]

The x-ray density of the composite was calculated from the molecular weight and x-ray density of the individual ferroic phases using the following relation[29]:

$$\rho_X = \frac{m_{YBT} + m_{SHF}}{m_{YBT}\rho_{YBT} + m_{SHF}\rho_{SHF}} \rho_{YBT}\,\rho_{SHF}, \quad (6)$$

where m_{YBT} and m_{SHF} are the molecular weight and ρ_{YBT} and ρ_{SHF} are the x-ray density of YBT and SHF, respectively.

Dielectric Formalism

The real part of the dielectric constant (ε') and the AC conductivity (σ_{AC}) were calculated from the experimental dielectric data using the following empirical relations:

$$\varepsilon' = Cd/A\varepsilon_0, \quad (7)$$

$$\sigma_{AC} = \varepsilon'\varepsilon_0\omega \tan\,\delta, \quad (8)$$

where C is the capacitance, d is the thickness of the sample, A is the area of the sintered pellet, and tan δ is the dielectric loss.

Variation of Dielectric Constant and Dielectric Loss with Temperature for YBT and YBT–SHF Composite

The variation of the dielectric constant (ε') with temperature (from 20°C to 530°C) at different frequencies (from 100 Hz to 1 MHz) was studied for the composite and is depicted in Fig. 5. With increasing frequency, the peak in the permittivity shifted to higher temperature, suggesting a relaxor nature of the ferroelectric phase transition in YBT after composite formation. The relaxor nature of the ferroelectric phase transition is associated with local ionic size/charge disorder in perovskite solid solutions.[30] However, pure YBT behaves like a normal ferroelectric with $T_c \sim 119$°C and does not exhibit relaxor feature, as shown in the inset of Fig. 5. A slight decrease of 4°C was observed for YBT compared with the value for pure BT (123°C) reported in earlier work.[15] The occupation of Y^{3+} ions at B site results in lattice expansion (as supported by the XRD results) and may suppress

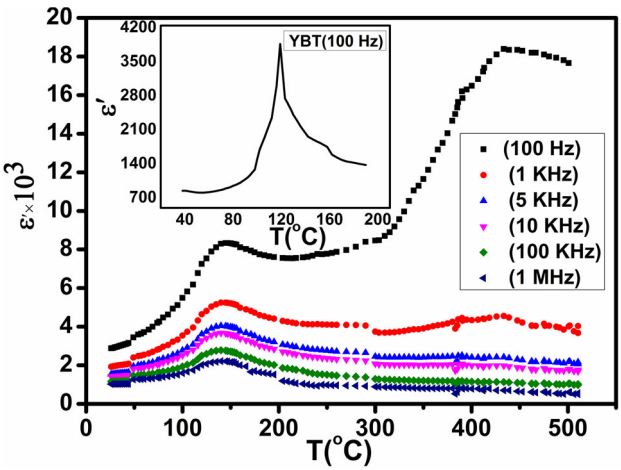

Fig. 5. Temperature dependence of dielectric constant of YBT–SHF composite; inset shows variation of dielectric constant with temperature for YBT phase.

oriented displacement of Ti^{4+} in the oxygen octahedrons, which is responsible for the spontaneous polarization. Therefore, the Curie temperature decreases with incorporation of Y^{3+} ions at Ti site.[31,32] All the transitions of the composite were diffuse. Similar diffuse-type transitions were also reported in literature for other ferroelectric–magnetic composites.[33] The increase in the transition temperature is due to internal stress resulting from the large-sized grains (especially greater than 1 μm)[34] and by diffusion of Fe^{2+} into the ferroelectric phase.[35] In the YBT–SHF composite, induced internal stresses are relieved due to the large size of the YBT grains ($\sim$ 4.81 μm). In addition, the high sintering temperature of 1150°C leads to diffusion of Fe^{2+} ions from the SHF phase into the ferroelectric YBT phase, causing T_c to shift towards higher temperature.

The temperature dependence of the loss tangent (tan δ) in the frequency range from 100 Hz to 1 MHz is shown in Fig. 6, while that of YBT at 100 Hz is shown in the inset. The dielectric loss was minimum at lower temperatures and increased with increase in temperature, similar to the behavior of the dielectric constant. Dielectric loss peaks were observed, shifting progressively towards higher temperature as the frequency was increased from 100 Hz to 1 MHz, which indicates a thermally activated relaxation mechanism. Similar dielectric

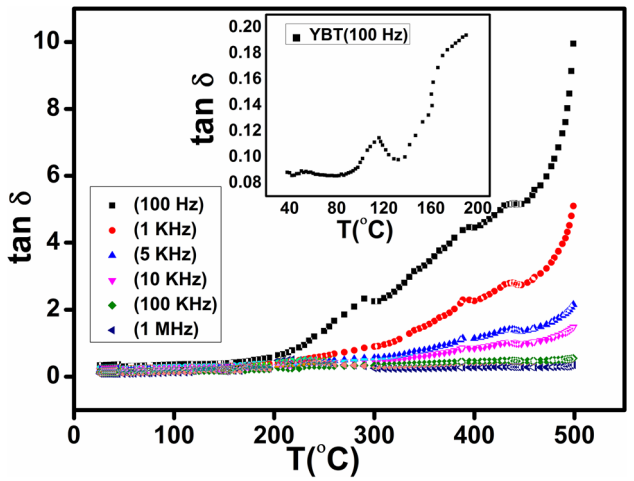

Fig. 6. Temperature dependence of tan δ of YBT–SHF composite; inset shows variation of tan δ with temperature for YBT phase.

loss behavior has been observed for various multiferroic composites, being explained on the basis of the Debye equation for loss.[36–38]

Curie–Weiss Behavior of YBT–SHF Composite

The diffuseness of the peak in the case of the YBT–SHF composite in the selected frequency range from 100 Hz to 1 MHz was confirmed using the modified Curie–Weiss law:

$$\frac{1}{\varepsilon'} - \frac{1}{\varepsilon'_{\max}} = A(T - T_c)^{\gamma}, \tag{9}$$

where $\varepsilon'_{\max}$ is the dielectric constant at T_c and γ is a critical exponent, lying in the range $1 < \gamma \leq 2$. $\gamma = 1$ represents ideal Curie–Weiss behavior, while a value between 1 and 2 indicates a diffuse transition.[39] The values of γ obtained from the slope of $\ln(1/\varepsilon' - 1/\varepsilon'_{\max})$ versus $\ln(T - T_c)$ for the YBT and YBT–SHF composite are depicted in Fig. 7. The obtained values of γ (Table II) confirm the diffuse transition for the composite.

Variation of Dielectric Constant and Dielectric Loss with Frequency for YBT and YBT–SHF Composite

The plot of ε' versus frequency for YBT and YBT–SHF is shown in Fig. 8. In comparison with the composite, the dielectric constant of YBT was small and hence is shown in the inset of Fig. 8. It was observed that ε' decreased with increase in frequency, showing dispersion in the lower frequency region (up to 10^3 Hz) and then approaching towards each other at frequency greater than 10^3 Hz. This effect is attributed to Maxwell–Wagner-type interfacial polarization.[40] The value of the dielectric constant ε' at lower frequency (20 Hz) for YBT and YBT–SHF was found to be 880 and 4127, respectively. This high dielectric constant value is the result of heterogeneous conduction, attributed to porosity in the material.[41] At frequencies greater than 10^5 Hz, the ε' values for YBT and YBT–SHF ran parallel and remained almost constant. The values of ε' observed at frequency of 3 MHz for YBT and YBT–SHF were 552 and 113, respectively. The abrupt decrease of ε' at higher frequencies is attributed to the fact that electron exchange between $Fe^{3+} \leftrightarrow Fe^{2+}$ does not follow the alternating electric field.

The variation of tan δ with frequency exhibited low-frequency dispersion (Fig. 9). The values of tan δ obtained at lower frequency (20 Hz) for YBT and YBT–SHF were 0.15 and 0.45, respectively. The dielectric loss at lower frequencies was negligible compared with our earlier results for BT-BHF [Barium titanate (BT)-Barium hexaferrite (BHF)] composite.[15] The reduction in the loss at lower frequencies may be due to the reduced space-charge polarization effect.[42] At higher frequency (3 MHz), the values of tan δ for YBT and YBT–SHF were 0.01 and 0.09, respectively. At higher frequencies, no charge diffusion occurs in the direction of the rapidly oscillating alternating electric field. This reduces charge accumulation and hence the value of tan δ. In addition, a loss peak was observed at frequency of 3.5 kHz for the YBT–SHF composite. This loss peak is attributed to the fact that the hopping frequency of electrons/holes among ions ($Fe^{3+} \leftrightarrow Fe^{2+}$) becomes equal to the frequency of the applied field.[42]

AC Conductivity of YBT–SHF Composite

The temperature dependence of the AC electrical conductivity (σ_{AC}) of YBT–SHF at selected frequencies is shown in Fig. 10. At low temperatures, σ_{AC} is proportional to temperature and is not activated in nature, as in semiconductors. Above T_c, an abrupt rise occurs in σ_{AC}, showing strong temperature dependence, with a hump observed near 140°C, supporting a ferroelectric transition.[43] As per the theoretical predictions, the change in slope occurs due to the transition of the sample from the ferro- to para-state when crossing the ferroelectric Curie temperature.[44]

The temperature dependence of σ_{AC} in ferrites, acting as one ferroic part of the composite, is due to both hopping of electrons and thermal excitation of electrons from the Fermi level to maximum density state, which can be expressed as[45]

$$\sigma_{AC} = \sigma_0 \exp^{E_0/k_B T} + \sigma_1 \exp^{E_1/k_B T} + \sigma_2 \exp^{E_2/k_B T} + \cdots \tag{10}$$

where E_0 is the activation energy for intrinsic conduction and E_1, E_2, etc. are the activation energies needed for hopping conduction. σ_0, σ_1, and σ_2 are constants, and k_B is Boltzmann's constant. The plot of $\ln(\sigma_{AC})$ versus $1000/T$ (Fig. 10) indicates two different slopes, characterizing electrical conduction via two different processes. The activation energy (E_a) values in the different

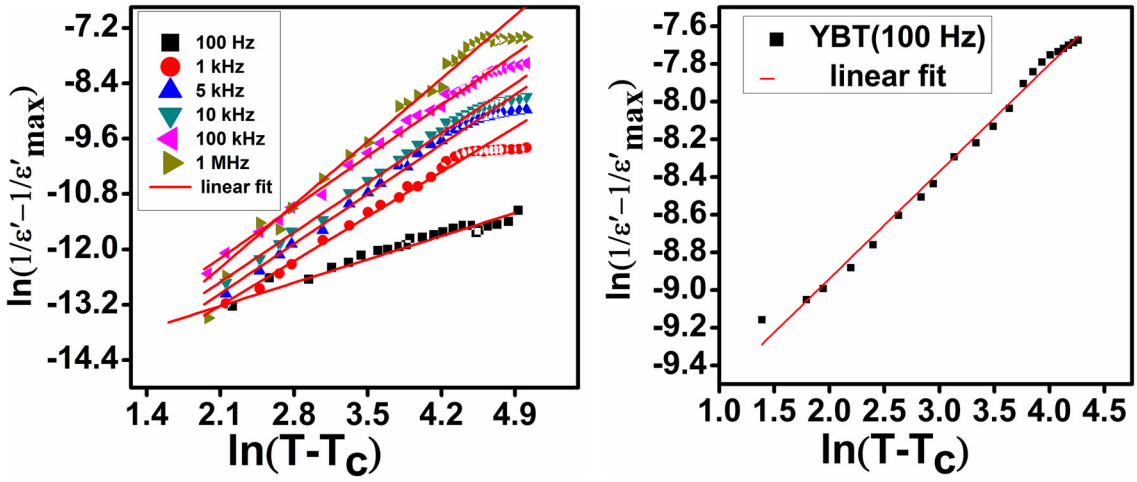

Fig. 7. Curie–Weiss behavior of (a) YBT–SHF composite at different frequencies and (b) YBT phase at 100 Hz.

Table II. Dielectric constant, Curie temperature, and activation energy for YBT–SHF composite at different frequencies

Sample	Frequency (Hz)	γ	ε'_{room}	ε'_{max}	T_c (°C)	Activation energy (eV) 520°C to 140°C	Activation energy (eV) 140°C to 20°C
YBT	100	0.58	850	3.85×10^3	119	–	–
YBT–SHF	100	1.21	2.86×10^3	8.33×10^3	138	1.04	0.01
–	10^3	1.37	2.02×10^3	5.24×10^3	140	0.79	0.01
–	5×10^3	1.53	1.71×10^3	4.04×10^3	141	0.62	0.01
–	10^4	1.54	1.48×10^3	3.63×10^3	143	0.35	0.02
–	10^5	1.58	1.25×10^3	2.77×10^3	144	–	–
–	10^6	1.95	0.95×10^3	2.21×10^3	145	–	–

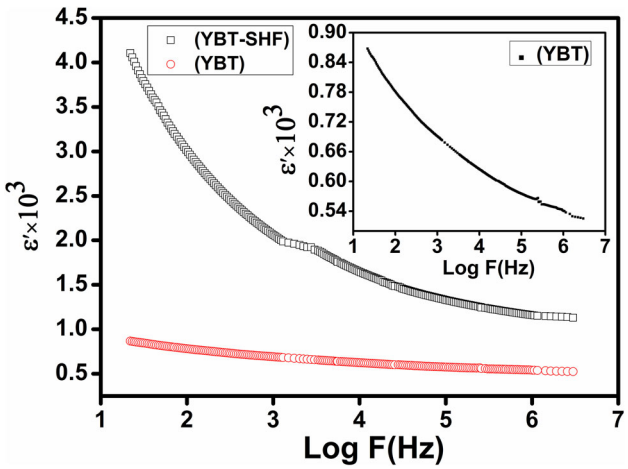

Fig. 8. Frequency dependence of dielectric constant of YBT–SHF composite; inset shows enlarged curve for YBT phase.

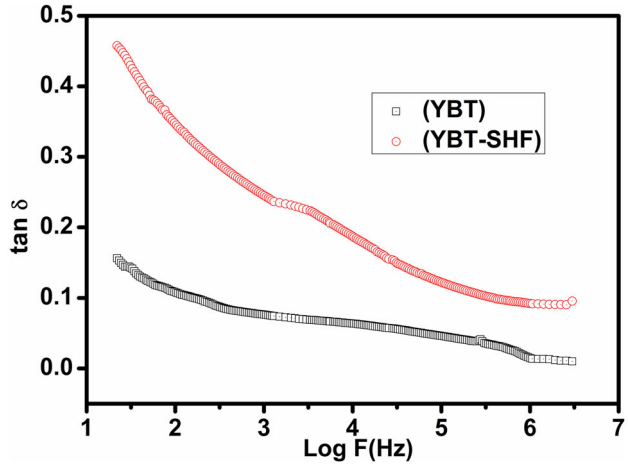

Fig. 9. Frequency dependence of dielectric loss of YBT phase and YBT–SHF composite.

temperature ranges from 520°C to 140°C and 140°C to 20°C were calculated. The values of E_1 calculated in the high temperature range (520°C to 140°C) were larger compared with E_0 obtained in the lower temperature range (140°C to 20°C). This decrease in activation energy with decreasing temperature can be attributed to small-polaron conduction.[45,46]

Furthermore, it is evident that the conductivity increased with increasing frequency. The frequency dependence of σ_{AC} is due to electron hopping

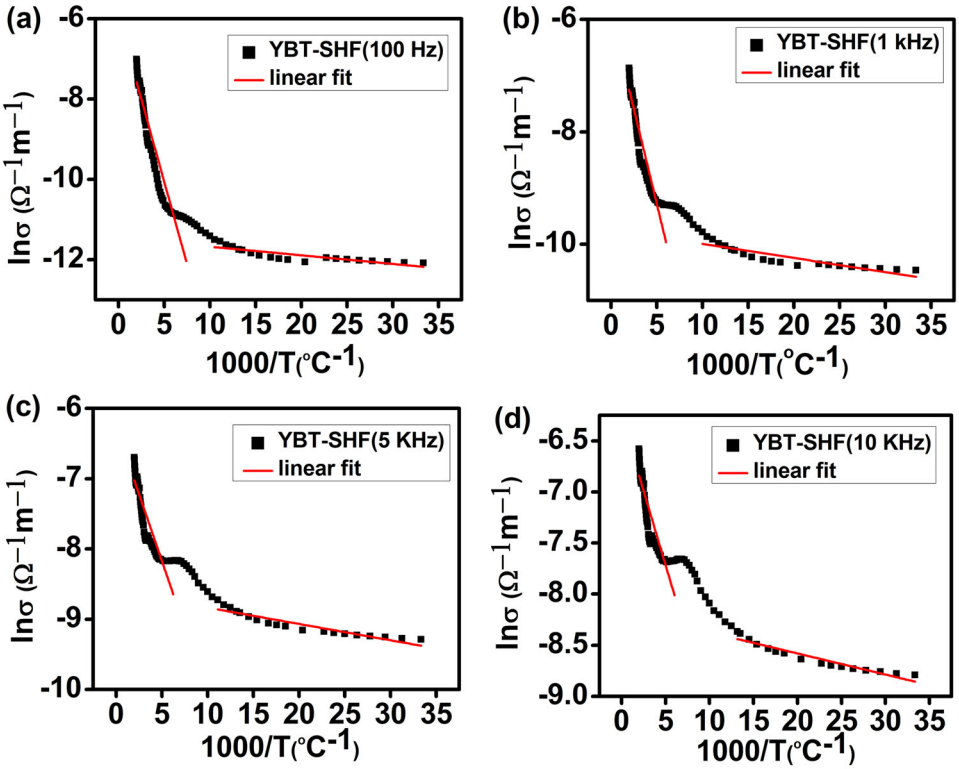

Fig. 10. Correlation between electrical conductivity (ln σ) and reciprocal of absolute temperature (1000/T) for YBT–SHF composite at (a) 100 Hz, (b) 1 kHz, (c) 5 kHz, and (d) 10 kHz.

between Fe^{2+} and Fe^{3+} ions in the ferrite phase of the composite. The observed increase in σ_{AC} with increasing frequency in the composite can be attributed to an increased hopping rate. A notable observation is that $E_a > 0.5$ eV for all frequencies, in support of the charge-hopping conduction mechanism in SHF, acting as one of the ferroic phases of the YBT–SHF composite.[47]

Ferroelectric Studies of YBT and YBT–SHF Composite

The symmetrical P–E hysteresis loops of the YBT–SHF composite (Fig. 11) confirmed its ferroelectric nature. The maximum polarization value of the composite was lower than that of YBT due to the presence of the conducting ferrite (SHF) in the composite. In addition, temperature-dependent hysteresis measurements were carried out for YBT to confirm the ferroelectric transition in YBT at temperature of 120°C (Fig. 12). The P–E loops for the YBT–SHF composite were traced by applying an electric field from 19.5 kV/cm to 24.42 kV/cm, revealing that all the loops were symmetrical about the origin. This symmetry of the loops can be attributed to the fact that the internal field developed by bound electrons is negligible compared with the externally applied field, which has not been reported previously for such composites.[14] The higher value of the coercive field in the YBT–SHF composite as compared with YBT is due to the clamping effect of SHF, which restricts domain switching.[48] On increasing the applied field, this clamping effect strengthens, increasing the coercive field as presented in Table III.

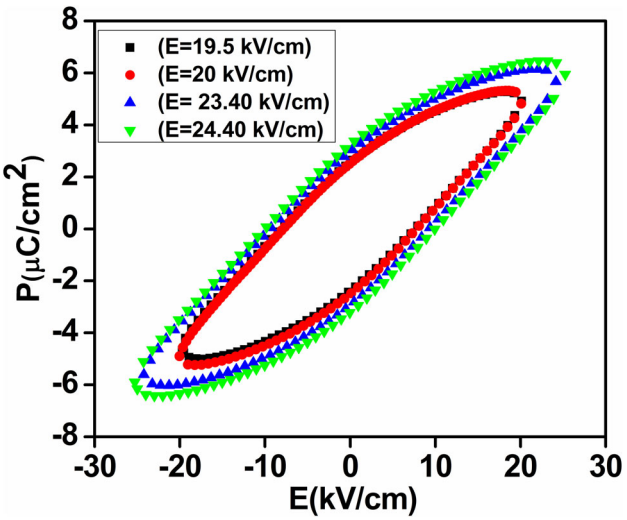

Fig. 11. Symmetrical P–E loops of YBT–SHF composite at different fields.

Magnetic Studies

The magnetic field dependence of the magnetization (M–H hysteresis loop) of SHF and the YBT–

SHF composite at room temperature is shown in Fig. 13. Typical magnetic hysteresis with saturation magnetization near field of 10 kOe was observed in both cases, confirming an ordered domain structure. The magnetic behavior of the composite is due to the ferrite phase.[49] The reason for the ferrimagnetic behavior of the composite is attributed to superexchange interactions ($Fe^{3+} \leftrightarrow O^{2-} \leftrightarrow Fe^{3+}$), enhanced by oxygen vacancies. Oxygen vacancies are created in the ferroelectric phase of the composite by substitution of Y^{3+} ion at Ti^{4+} site,[22] a mechanism that can be expressed in Kröger–Vink notation as[50,51]

$$Y_2O_3 + 2BaO \rightarrow Y'_{Ti} + 2Ba_{Ba} + 5Oo + V_o^{\cdot\cdot}$$

Table I presents the values obtained for the various magnetic parameters. The magnetic moment per formula unit in Table I was calculated using the following formula[50]:

$$n_B = \frac{M \times M_s}{5585}, \quad (11)$$

where M and M_s are the molecular weight and saturation magnetization of a particular composition.

The values of M_s and M_r obtained for the composite were lower than those of the SHF phase. This is attributed to the presence of the nonmagnetic ferroelectric YBT phase, which may dilute various magnetic properties in the composite.[51] Furthermore, the magnetic dilution with the change of Fe^{3+} (high-spin state) to Fe^{2+} (low-spin state) at 2a site of $SrFe_{12}O_9$ on substitution of Y^{3+} ions at Sr^{2+} site and the effect of spin canting may be responsible for weakening the superexchange fields.[52] The $Fe^{3+} \leftrightarrow O^{2-} \leftrightarrow Fe^{3+}$ exchange interaction is disrupted by Fe^{2+} ion canted spins, which could be produced by substitution of Y^{3+} ion into the SHF phase during high-temperature sintering.[52,53] In addition, the

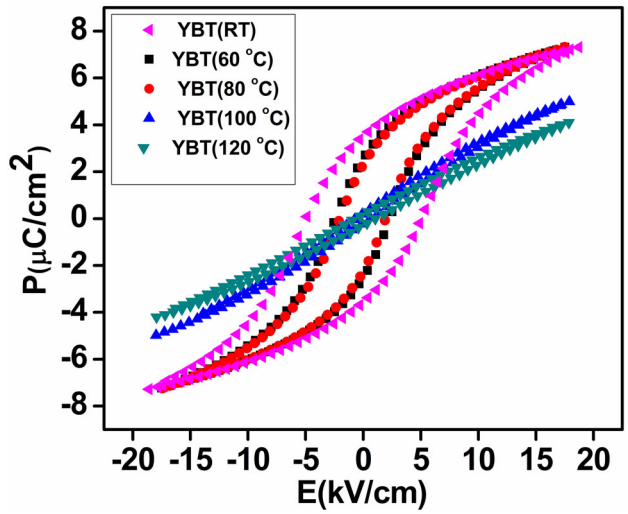

Fig. 12. Typical *P*–*E* loops of YBT phase at different temperatures.

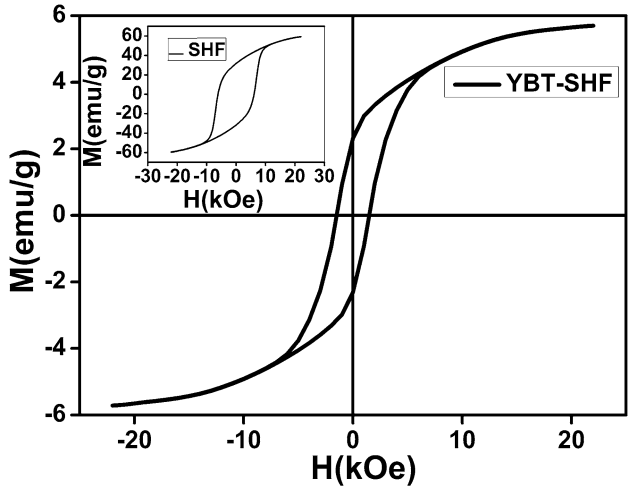

Fig. 13. *M*–*H* hysteresis loop of YBT–SHF composite; inset shows *M*–*H* hysteresis of SHF phase.

Table III. Variation of ferroelectric parameters of YBT phase with temperature and of YBT–SHF composite with applied field

Sample	T (°C)	P_{max} (μC/cm^2)	E_c (kV/cm)	P_r (μC/cm^2)	Applied field (kV/cm)
YBT	RT	7.52	5.07	3.49	–
YBT	50	7.41	2.31	2.53	–
YBT	75	7.28	1.93	2.18	–
YBT	105	5.5	1.05	0.90	–
YBT	120	3.9	0.42	0.12	–
YBT–SHF	RT	6.48	10.23	3.23	24
YBT–SHF	RT	6.11	9.39	2.99	22
YBT–SHF	RT	2.62	7.88	2.62	20
YBT–SHF	RT	2.50	7.72	2.50	19

RT, room temperature.

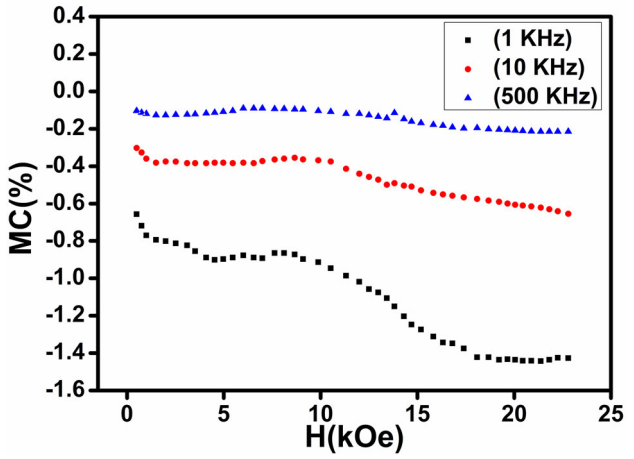

Fig. 14. Variation of magnetocapacitance with magnetic field for YBT–SHF composite at different frequencies.

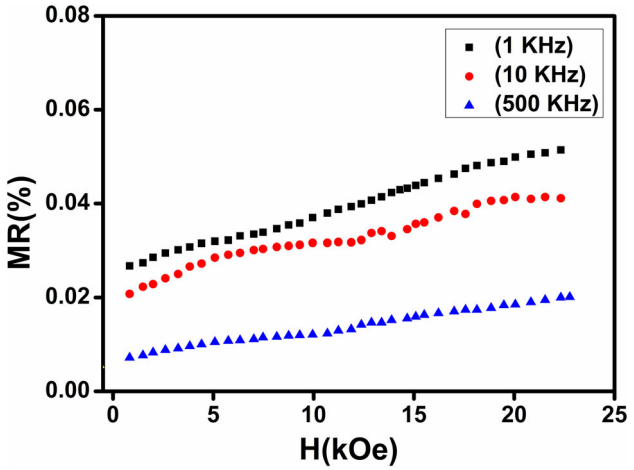

Fig. 15. Variation of magnetoresistance with magnetic field for YBT–SHF composite at different frequencies.

coercive field of the composite was found to be lower than that of SHF phase, confirming easy magnetic domain wall motion and rotation of dipoles in SHF, compared with the composite.[54] In addition, the maximum coercivity for SHF phase occurred within its single-domain range, as supported by the squareness ratio (M_r/M_s) of 0.55 in Table I. However, decreased coercivity arises in the composite as grains are subdivided into multiple domains (M_r/M_s = 0.40).

Magnetocapacitance Studies

The phenomenon of magnetocapacitance (MC) in composites, which is an indirect way to investigate the magnetoelectric effect, arises due to mechanical coupling between two ferroic phases. Application of a magnetic field changes not only the magnetic order but also the electric permittivity.[55] When a magnetoelectric composite is subjected to a magnetic field, it

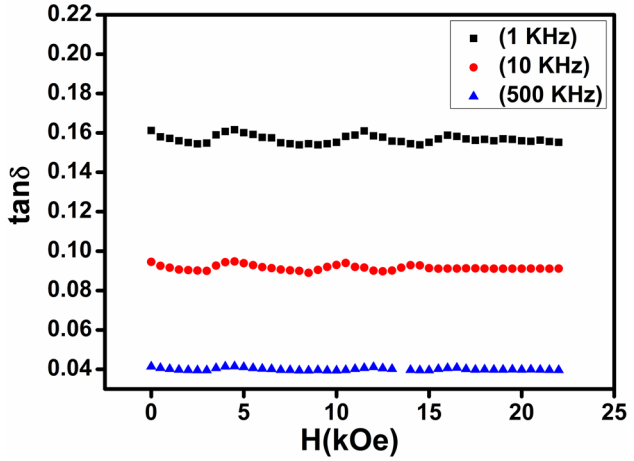

Fig. 16. Variation of tan δ with magnetic field for YBT–SHF composite at different frequencies.

becomes strained. The generated strain induces stress, which is transferred to the ferroelectric phase of the composite, resulting in an electric field across ferroelectric domain walls.[56]

The MC effect in the YBT–SHF composite was checked by measuring the change in capacitance as a function of external magnetic field in the frequency range from 1 kHz to 500 kHz. The MC was calculated using the following formula:

$$\mathrm{MC} = \frac{\varepsilon(H) - \varepsilon(H=0)}{\varepsilon(H=0)} \times 100, \qquad (12)$$

where $\varepsilon(H)$ and $\varepsilon(H = 0)$ are the dielectric constant in the presence and absence of magnetic field, respectively. In the present study, the MC showed weak dependence on the magnetic field at higher frequency, but a significant response was observed at lower frequency (Fig. 14). The MC of the YBT–SHF composite was found to be 0.77%, 0.35%, and 0.11% at 1 kHz, 10 kHz, and 500 kHz, respectively. These low values are due to the lower content of SHF in the composite. The MD response at frequencies below 10 kHz is due to a favorable magnetoresistance (MR) effect combined with the Maxwell–Wagner effect.[55] The MR of the composite, viz. the fractional change in resistivity on application of a magnetic field, can be evaluated using the following relation:

$$\mathrm{MR} = \frac{\rho(H) - \rho(H=0)}{\rho(H=0)} \times 100. \qquad (13)$$

The change in the MR and tan δ with the applied magnetic field from 0 kOe to 20 kOe is depicted in Figs. 15 and 16, respectively. It is clear that the slight increase in MR (0.03%) at lower frequency (1 kHz) is responsible for the MD effect in the composite. The favorable MD response supported by this enhancement in the resistance is attributed to good interfacial connection between the two ferroic phases.[57] The dielectric loss of the composite under

the influence of a magnetic field was almost constant for all frequencies.

CONCLUSIONS

Morphological studies revealed monophasic structure for YBT and SHF, while biphasic structure was observed for the YBT–SHF composite. XRD analysis confirmed that the individual phases retained their crystal structure in the composite. Density calculations revealed porosity in the material, consistent with the morphology. Enhancement in the dielectric constant due to yttrium doping and a diffuse transition were observed for the composite. The ferroelectric loops of YBT confirmed its ferroelectric transition at high temperature, while the typical hysteresis of the YBT–SHF composite at different fields confirmed its ferroelectric nature. Activation energies calculated in two different temperature regions confirmed the charge-hopping mechanism in the composite. The magnetic hysteresis loops of the composite confirmed that the magnetic parameters were diluted due to the presence of the nonmagnetic YBT phase. Magnetodielectric studies confirmed the contribution of magnetoresistance to the magnetodielectric phenomenon.

ACKNOWLEDGEMENT

The authors are grateful to the authorities of the University of Kashmir for providing the vibrating-sample magnetometer facility (MicroSense EZ9 VSM) to the Department of Physics under a DST, Government of India special package for sophisticated instrumentation.

REFERENCES

1. M. Fiebig, Th Lottermoser, D. Frohlich, A.V. Goltsev, and R.V. Pisarev, *Nature (London)* 419, 818 (2002).
2. J. Wang, J.B. Neaton, H. Zheng, V. Nagarajan, S.B. Ogale, B. Liu, D. Viehland, V. Vaithyanathan, D.G. Schlom, U.V. Waghmare, N.A. Spaldin, K.M. Rabe, M. Wuttig, and R. Ramesh, *Science* 299, 1719 (2003).
3. T. Kimura, T. Goto, H. Shintani, K. Ishizaka, T. Arima, and Y. Tokura, *Nature (London)* 426, 55 (2003).
4. N.A. Spaldin and M. Fiebig, *Science* 309, 391 (2005).
5. J.F. Scott, *Nat. Mater.* 6, 256 (2007).
6. N. Hur, S. Park, P.A. Sharma, J.S. Ahn, S. Guha, and S.W. Cheong, *Nature* 429, 392 (2004).
7. H. Schmid, *Bull. Mater. Sci.* 17, 1411 (1994).
8. C.W. Nan, *Phys. Rev. B* 50, 6082 (1994).
9. S.D. Chavan, S.G. Chavan, S.S. Mane, P.B. Joshi, and D.J. Salunkhe, *J. Mater. Sci. Mater. Electron.* 27, 1258 (2016).
10. I.B. Shameem Banu, A. Sathiya Priya, P. Komalavalli, and G. Shanmuganathan, *J. Mater. Sci. Mater. Electron.* 26, 101 (2015).
11. A. Srinivasa, T. Karthik, R. Gopalan, and V. Chandrasekarana, *Mater. Sci. Eng. B* 172, 289 (2010).
12. A.M.J.G. Run, D.R. Terrell, and J.H. Scholing, *J. Mater. Sci.* 9, 1710 (1974).
13. G. Srinivasan, E.T. Rasmussen, B.J. Levin, and R. Hayes, *Phys. Rev. B* 65, 134402 (2002).
14. Robert C. Pullar, *ACS Comb. Sci.* 14, 425 (2012).
15. B. Want, M.D. Rather, and R. Samad, *J. Mater. Sci. Mater. Electron.* 27, 5860 (2016).
16. X.H. Zhu, J. Li, and D.N. Zheng, *Appl. Phys. Lett.* 90, 142913 (2007).
17. W. Li, J.G. Hao, W.F. Bai, Z.J. Xu, R.Q. Chu, and J.W. Zhai, *J. Alloys Compd.* 531, 46 (2012).
18. P.K. Patel and K.L. Yadav, *Phys. B* 442, 39 (2014).
19. O. Umit, A. Yahya, and M. Hadis, *J. Mater. Sci. Mater. Electron.* 20, 789 (2009).
20. J. Zhang, J. Fu, F. Li, E. Xie, D. Xue, N.J. Mellors, and Y. Peng, *ACS Nano* 6, 2273 (2012).
21. X. Meng, J. Mi, Q. Li, C. Bortolini, and M. Dong, *Mater. Res. Express* 1, 036106 (2014).
22. P.K. Patel and K.L. Yadav, *Phys. B* 442, 39 (2014).
23. S. Bhaskar Reddy, M.S. Ramachandra Rao, and K. Prasad Rao, *Appl. Phys. Lett.* 91, 022917 (2007).
24. M. Fechner, S. Ostanin, and I. Mertig, *Phys. Rev. B* 77, 094112 (2008).
25. P. Ren, Q. Wang, X. Wang, L. Wang, J. Wang, H. Fan, and G. Zhao, *Mater. Lett.* 174, 197 (2016).
26. G.E. Manger, *Porosity and Bulk Density of Sedimentary Rocks*, serial no. 1144, chap. E (Geological Survey Bulletin, Washington, 1963), pp. E1–E55.
27. M.J. Iqbal and M.N. Ashiq, *Chem. Eng. J.* 136, 383 (2008).
28. J. Saggio-Woyansky and C.E. Scott, *Am. Ceram. Soc. Bull.* 71, 1674 (1999).
29. A.D. Shaikh and V.L. Mathe, *Smart Mater. Struct.* 18, 065014 (2009).
30. A.A. Bokov and Z.G. Ye, *J. Mater. Sci.* 41, 31 (2006).
31. Y. Wang, L. Li, J. Qi, and Z. Gui, *Ceram. Int.* 28, 657 (2002).
32. X.J. Chou, J.W. Zhai, H.T. Jiang, and X. Yao, *J. Appl. Phys.* 102, 084106 (2007).
33. B.K. Bammannavar and L.R. Naik, *Smart Mater. Struct.* 18, 085013 (2009).
34. Y. Zhi and A. Chen, *J. Appl. Phys.* 9, 794 (2002).
35. R. Maier, J.L. Chon, J.J. Neumeier, and L.A. Bendersky, *Appl. Phys. Lett.* 78, 2536 (2001).
36. S.S. Chougule and B.K. Chougule, *Mater. Chem. Phys.* 108, 408 (2008).
37. B.K. Bammannavar and L.R. Naik, *Smart Mater. Struct.* 18, 085013 (2009).
38. L.L. Hench and J.K. West, *Principles of Electronic Ceramics* (New York: Wiley, 1990), p. 189.
39. Z.Q. Zhuang, M.P. Harmer, D.M. Smyth, and R.E. Newnham, *Mater. Res. Bull.* 22, 1329 (1987).
40. K.W. Wagner, *Ann. Phys.* 40, 818 (1993).
41. C.A. Guarany, L.H.Z. Pelaio, E.B. Araujo, K. Yukimitu, J.C. Moraes, and J.A. Eiras, *J. Phys. Condens. Matter* 15, 4851 (2003).
42. M.A. Ahmed and E.H. El-Khawas, *Indian J. Phys. A* 74A, 497 (2000).
43. D.K. Kulkarni and C.S. Prakash, *Bull. Mater. Sci.* 17, 35 (1994).
44. Y.P. Kin and E.A. Turov, *Fiz. Met. Metalloved.* 4, 95 (1957).
45. S. Ambily and C.S. Menon, *Thin Solid Films* 347, 284 (1999).
46. N.F. Mott and E.A. Davis, *Electronic Processes in Non-Crystalline Materials*, 2nd edn, Clarendon: Oxford, 1972), p. K55.
47. K. Kamala Bharathi, G. Markandeyulu, and C.V. Ramana, *Solid State Lett.* 13, 98 (2010).
48. H. He, J. Ma, J. Wang, and C.W. Nan, *J. Appl. Phys.* 103, 034103 (2008).
49. L.P. Curecheriu, M.T. Buscaglia, V. Buscaglia, L. Mitoseriu, P. Postolache, A. Ianculescu, and P. Nanni, *J. Appl. Phys.* 107, 104106 (2010).
50. J. Smit and H.P.J. Wijn, *Adv. Electron. Electron. Phys.* 6, 69 (1954).
51. P.A. Jadhav, M.B. Shelar, and B.K. Chougule, *J. Alloys Compd.* 479, 385 (2009).
52. X. Liu, W. Zhong, S. Yang, Z. Yu, B. Gu, and Y. Du, *Phys. Status Solidi (a)* 193, 314 (2002).

53. X. Liu, W. Zhong, S. Yang, Z. Yu, B. Gu, and Y. Du, *J. Magn. Magn. Mater.* 238, 207 (2002).
54. L. Zhang, J. Zhai, W. Mo, and X. Yao, *Solid State Sci.* 13, 321 (2011).
55. G. Catalan, *Appl. Phys. Lett.* 88, 102902 (2006).
56. S.N. Babu, J.H. Hsu, Y.S. Chen, and J.G. Lin, *J. Appl. Phys.* 109, 07D904 (2011).
57. Y. Shen, J. Sun, L. Li, Y. Yao, C. Zhou, R. Su, and Y. Yang, *J. Mater. Chem. C* 2, 2545 (2014).